

Mineralogy and thermal properties of V-type Asteroid 956 Elisa: Evidence for diogenitic material from the Spitzer IRS (5–35 μm) spectrum

Lucy F. Lim^{a,*}, Joshua P. Emery^b, Nicholas A. Moskovitz^{c,d}

^a NASA/Goddard Space Flight Center, Greenbelt, MD 20771, United States

^b Earth and Planetary Science Department, University of Tennessee, Knoxville, TN 37996, United States

^c Institute for Astronomy, University of Hawaii, Honolulu, HI 96822, United States

^d Carnegie Institution of Washington, Department of Terrestrial Magnetism, Washington, DC 20015, United States

ARTICLE INFO

Article history:

Received 30 December 2009

Revised 3 December 2010

Accepted 3 December 2010

Available online 11 December 2010

Keywords:

Asteroids, Composition

Asteroids, Surfaces

Spectroscopy

Mineralogy

Infrared observations

ABSTRACT

We present the thermal infrared (5–35 μm) spectrum of 956 Elisa as measured by the Spitzer Infrared Spectrograph (“IRS”; Houck, J.R. et al. [2004]. *Astrophys. J. Suppl.* 154, 18–24) together with new ground-based lightcurve data and near-IR spectra. From the visible lightcurve photometry, we determine a rotation period of 16.494 ± 0.001 h, identify the rotational phase of the Spitzer observations, and estimate the visible absolute magnitude (H_V) at that rotational phase to be 12.58 ± 0.04 . From radiometric analysis of the thermal flux spectrum, we find that at the time of observation 956 Elisa had a projected radius of 5.3 ± 0.4 km with a visible albedo $p_V = 0.142 \pm 0.022$, significantly lower than that of the prototype V-type asteroid, 4 Vesta. (This corresponds to a radius of 5.2 ± 0.4 km at lightcurve mean.) Analysis with the standard thermal model (STM) results in a sub-solar temperature of 292.3 ± 2.8 K and beaming parameter $\eta = 1.16 \pm 0.05$. Thermophysical modeling places a lower limit of $20 \text{ J m}^{-2} \text{ K}^{-1} \text{ s}^{-1/2}$ on the thermal inertia of the asteroid’s surface layer (if the surface is very smooth) but more likely values fall between 30 and $150 \text{ J m}^{-2} \text{ K}^{-1} \text{ s}^{-1/2}$ depending on the sense of rotation.

The emissivity spectrum, calculated by dividing the measured thermal flux spectrum by the modeled thermal continuum, exhibits mineralogically interpretable spectral features within the 9–12 μm reststrahlen band, the 15–16.5 μm Si–O–Si stretching region, and the 16–25 μm reststrahlen region that are consistent with pyroxene of diogenitic composition: extant diogenitic pyroxenes fall within the narrow compositional range $\text{Wo}_{2\pm1}\text{En}_{7.4\pm2}\text{Fs}_{24\pm1}$. Spectral deconvolution of the 9–12 μm reststrahlen features indicates that up to $\approx 20\%$ olivine may also be present, suggesting an olivine-diogenite-like mineralogy. The mid-IR spectrum is inconsistent with non-cumulate eucrite as the major component on the surface of 956 Elisa, although cumulate eucrite material may be present at abundances lower than that of the diogenite component.

Analysis of new near-IR spectra of 956 Elisa with the Modified Gaussian Model (MGM; Sunshine, J.M., Pieters, C.M., Pratt, S.F. [1990]. *J. Geophys. Res.* 95 (May), 6955–6966) results in two pyroxene compositions: 75% magnesian low-Ca pyroxene and 25% high-Ca pyroxene. High-Ca pyroxene is not evident in the mid-IR data, but may belong to a component that is underrepresented in the mid-IR spectrum either because of its spatial distribution on the asteroid or because of its particle size. High-Ca pyroxenes that occur as exsolution lamellae may also be more evident spectrally in the NIR than in the mid-IR. In any case, we find that the mid-IR spectrum of 956 Elisa is dominated by emission from material of diogenite-like composition, which has very rarely been observed among asteroids.

Published by Elsevier Inc.

1. Introduction

The dynamical family of small basaltic asteroids associated with 4 Vesta (“Vestoids”; Binzel and Xu, 1993) is considered to be the proximate source of the HED (howardite, eucrite, and diogenite) meteorites. The majority of these meteorites are thought to have

* Corresponding author.

E-mail address: lucy.f.lim@nasa.gov (L.F. Lim).

their ultimate origin on Vesta itself (McCord et al., 1970; Consolmagno and Drake, 1977). Hubble Space Telescope imaging of Vesta (Thomas et al., 1997a) has revealed an impact basin large enough ($D \approx 460$ km) to be the source of all known Vestoids. Spectral studies of Vestoids in the visible and near-IR have characterized their olivine and pyroxene compositions and revealed significant differences between HED and Vestoid populations. For example, about 25% of HED meteorites are diogenites, although to date, observations of diogenite-like near-IR spectra among Vestoids have been

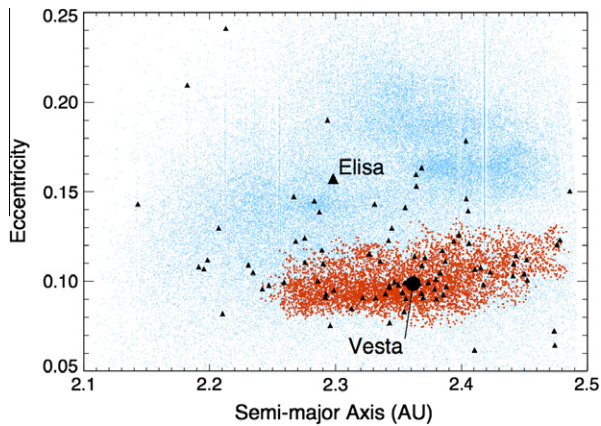


Fig. 1. Proper elements of 956 Elisa in the context of 4 Vesta and its dynamical family. The small dots represent all known asteroids; dark filled circles are Vesta's dynamical family; and the large filled black dot represents 4 Vesta. The small filled triangles are all spectroscopically confirmed V-types.

very rare. A number of vestoids (Burbine et al., 2001; Duffard et al., 2004) have been characterized as having olivine-rich compositions long unrepresented among meteorites. (Recently, however, the meteorite MIL 03443 has been suggested (Mittlefehldt, 2008) to be a dunite sample from the HED parent body.) Similar NIR features suggest regional olivine exposures on Vesta itself (Gaffey, 1997; Binzel et al., 1997).

The inner-main-belt Asteroid 956 Elisa was identified as a V-type asteroid by Florczak et al. (2002), who considered it to be outside the limits of the Vesta dynamical family although it is relatively close to the Vestoids in proper element space (Fig. 1). Subsequently, however, numerous other V-type asteroids were discovered in the inner-main-belt outside the boundaries of the Vesta family. A dynamical mechanism was proposed by which 956 Elisa could have been transported to its present orbit from within the Vesta family (Carruba et al., 2005, 2007), and 956 Elisa's orbit is now generally considered consistent with an origin on 4 Vesta (Nesvorný et al., 2008).

We present the thermal infrared (5–35 μm) spectrum of 956 Elisa as measured by the Spitzer Infrared Spectrograph ("IRS"; Houck et al., 2004) together with new measurements of the visible lightcurve and near-infrared (0.8–2.5 μm) spectrum. The thermal flux spectrum, with constraints provided by the absolutely calibrated visible lightcurve, provides new estimates of the radius, thermal inertia, and albedo. The lightcurve data also permit accurate determination of a rotation period for 956 Elisa. Mid-IR spectral emissivity features are also observed in the spectrum of Elisa: comparison with laboratory spectra of relevant samples, including HED meteorites, establishes that these features are diagnostic of mineralogy and permits the determination of a pyroxene composition for 956 Elisa. The near-IR spectrum is used to independently estimate the surface composition of 956 Elisa, and the results of the two techniques are compared.

2. Circumstances of the Spitzer observations

Spectra of 956 Elisa were acquired on 2008-August-02 in the four low-resolution orders of the Spitzer IRS (Houck et al., 2004). All observations were completed between UT 18:03:50 and UT 18:26:26. During the observation, 956 Elisa was at $R = 1.832$ AU, $\Delta = 1.110$ AU, and a phase angle of 29.32° .¹ The acquisition mode

¹ Following convention, we use R to represent the asteroid–Sun distance and Δ to represent the asteroid–observer distance. In this case, the observer is at the location of the Earth-trailing Spitzer observatory rather than on Earth.

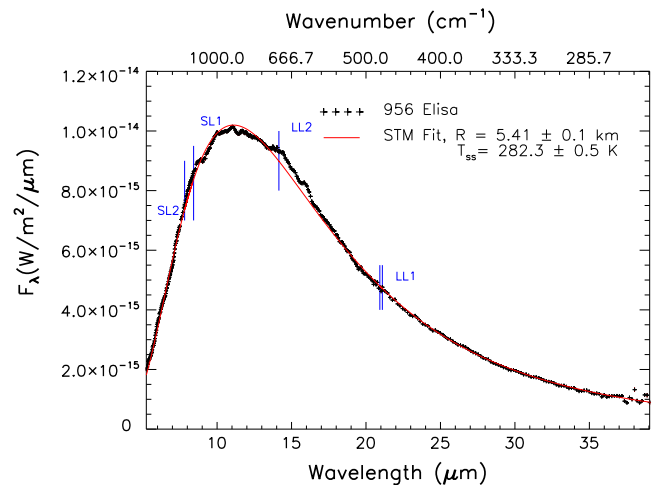


Fig. 2. Spitzer IRS spectrum of 956 Elisa with standard thermal model ("STM") fit overlaid. The wavelength ranges of the four Spitzer low-resolution orders (SL2, SL1, LL2, LL1) are marked in blue. Data from the four orders were spliced together to assemble this composite spectrum. The scaling factors were: +1.12% (SL2/SL1), −0.84% (LL2/SL1), and −4.47% (LL1/SL1). Of these, the LL2/SL1 (14.15 μm) is the most uncertain due to an IRS instrumental artifact (Section 3.2) that sporadically produces excess flux in the 13.5–14.15 μm region of SL1, immediately shortward of the LL2 boundary. Thus, we have incorporated an additional 2.5% uncertainty in this value into our radius and temperature solutions. (For interpretation of the references to colour in this figure legend, the reader is referred to the web version of this article.)

of the IRS was very similar to standard ground-based spectroscopy in that the asteroid was observed at two nod positions approximately 1/3 and 2/3 of the length of the slit.

Much of the data reduction was carried out at the Spitzer Science Center (SSC) by pipeline processing. Data were returned to the observers as flat-fielded, flux-calibrated spectral images. We removed background emission by subtracting frames from the two nod positions, corrected for rogue pixels using software supplied by the SSC (<http://ssc.spitzer.caltech.edu/postbcd/irs-clean.html>), and extracted the 1-D spectra using SPICE, another piece of software supplied by the SSC (<http://ssc.spitzer.caltech.edu/postbcd/spice.html>). For Elisa, we had obtained multiple cycles for each of the four modules at both nod positions. We averaged all cycles and both nod positions to produce a final spectrum for each module. The four modules were scaled relative to each other using flux densities in wavelength regions of overlap. The entire spectrum was then rescaled to the average flux of the four segments, conserving the measured photometric flux. The scaling factors in all cases fell within the 5% per order photometric flux uncertainties of the IRS.

3. Thermal model fitting: radius and temperature

In the 5–38 μm region, the spectrum of 956 Elisa is dominated by thermal emission. To model the thermal continuum of 956 Elisa (Fig. 2), we apply a variant of the Standard Thermal Model ("STM"; Lebofsky et al., 1986; Spencer et al., 1989) to the IRS emission spectra of the asteroid. The STM begins with the assumption that the asteroid is a spherical greybody in equilibrium with the incoming solar radiation at every point on its surface:

$$T(\theta) = T_{\max} \cos^{1/4}(\theta) \quad (1)$$

where θ is the angular distance between any point on the sunlit side of the asteroid and the sub-solar point.

The thermal flux from the surface is then calculated by integrating the Planck function over the projected surface area of the object. For a spherical body, this can be expressed as

$$F(\lambda) = \frac{r^2}{\Delta^2} \epsilon(\lambda) \int_{\theta} B(\lambda, T(\theta)) \cos(\theta) \sin(\theta) d\theta \quad (2)$$

where r is the asteroid radius, $\epsilon(\lambda)$ is the emissivity, and $B(\lambda, T)$ is the Planck function. The two free parameters in this model, radius and maximum (sub-solar point) temperature, are varied to fit the measured flux. In this relatively simple model, other factors such as albedo and beaming parameter are calculated directly from the radius and sub-solar point temperature. The particular strength of the IRS data for thermal modeling is the broad and continuous wavelength coverage from 5.2 to 38 μm that includes the thermal emission peak for asteroids. The temperature is tightly constrained by the shape of the spectrum and the size by the absolute flux level.

3.1. Radius estimate

While the procedure for estimating size is relatively straightforward, several sources of uncertainty related to the absolute flux of the spectrum and some model parameters must be considered to assess the accuracy of the result.

The formal error in the radius resulting from the fitting procedure based on the relative uncertainties of the Spitzer data points is quite small, ± 0.1 km. Other sources of error dominate the overall uncertainty in our radius estimate. The most important are the absolute flux uncertainties in the Spitzer IRS data ($\pm 5\%$ per order, thus $\pm 2.5\%$ for the average of the four orders), uncertainties in the scaling between the orders ($\pm 2.5\%$), and the thermal IR phase correction.

The thermal IR phase correction can be made either with a phase coefficient which is constant with wavelength, established empirically as 0.01 ± 0.005 mag./ $^\circ$ (Spencer et al., 1989; Matson, 1972); or by the NEATM method (Harris, 1998) in which the portion of the asteroid out of the field of view is eliminated directly from the STM flux calculation. In other words, the original STM integrates thermal flux at zero phase angle over the sunlit hemisphere and then decreases the flux by 0.01 mag./ $^\circ$ to the phase angle of the observation. The NEATM, on the other hand, integrates the flux directly at the phase angle of the observation over the visible hemisphere ($T = 0$ K on the nightside) as seen by the observer. The difference in final flux between the two phase curves depends strongly on phase angle and for moderate phase angles ($< 70^\circ$) peaks at 13–20% around 25–40 $^\circ$.

Examination of the infrared phase curve of Ceres, for instance (Spencer, 1990) reveals that the NEATM provides a better match to the pre-opposition phase curve, but the 0.01 mag./ $^\circ$ is a better model for the post-opposition phase curve. Thus, neither model can be established to be universally more accurate.

Because of the high phase angle (29.319 $^\circ$) of the Spitzer observation, the ± 0.005 mag./ $^\circ$ cited uncertainty in the IR phase curve produces the largest component in the uncertainty of our radius calculation: +7.0%/–6.5% in radius. (At this angle, the NEATM produces a phase correction equivalent to the lower range of the STM, 0.005 mag./ $^\circ$, so the STM/NEATM variation is included within this range.)

As shown in Eq. (2), the integrated flux depends equally on r^2 and bolometric emissivity. Uncertainties in the assumed emissivity will therefore propagate to the derived radius. The effective emissivity of a silicate asteroid with the surface temperature distribution of 956 Elisa can be calculated based on the emissivity data in the ASU library (Christensen et al., 2000):

$$\epsilon_{\text{effective}} = \frac{\int_{\lambda} F_{\text{STM}}(\lambda) \epsilon(\lambda) d\lambda}{\int_{\lambda} F_{\text{STM}}(\lambda) d\lambda} \quad (3)$$

Assuming that the asteroid's composition is 50–100% pyroxene and 0–50% plagioclase, the effective emissivity will be $92.6\% \pm 1.7\%$. The

corresponding contribution to the uncertainty in the radius estimate is 0.9%.

Overall, we estimate that the projected radius of 956 Elisa at the time of the Spitzer observation was 5.3 ± 0.4 km.

3.2. Temperature estimate

In the STM and NEATM, the temperature distribution of the asteroid's surface is a function of the maximum temperature (Eq. (1)). The maximum temperature from the thermal fit, T_{max} , is subject to fewer sources of uncertainty than the radius estimate. Essentially, factors that change the shape of the measured or modeled spectrum will affect the temperature determination. The relative (point-to-point) spectral uncertainty contributes only a negligible amount to the temperature uncertainty. An inherent wavelength dependence of the NEATM infrared phase curve is potentially responsible for a 1.1 K change in the temperature estimate; the uncertainties associated with splicing the four Spitzer IRS orders together may account for another 2.5 K. (Caution is especially required in considering the SL1/LL2 scaling, as the 14.15 μm region is close to an artifact known as the “14-micron teardrop” [“IRS: Image and Spectral Features”, <http://ssc.spitzer.caltech.edu/irs/features.html>] that appears sporadically in SL1.)

Including all of these uncertainties, we estimate the maximum temperature of 956 Elisa at the time of observation to have been $T_{\text{max}} = 282.3 \pm 2.8$ K.

The derived maximum temperature and size depend on the position of Elisa, which is well known for all of our observations, but also contains information about the albedo, effective emissivity, thermal inertia, and surface roughness of the asteroid:

$$T_{\text{max}} = \left[\frac{(1 - A)(\text{insolation})}{\eta \epsilon \sigma} \right]^{\frac{1}{4}} \quad (4)$$

where A is the Bond albedo, σ is the Stefan–Boltzmann constant, ϵ is the effective emissivity, and η is the “beaming parameter”, which represents a combination of the thermophysical properties of the surface (e.g. thermal inertia) and the surface roughness.

In order to isolate these factors from one another, additional information such as reflected-light (visible or NIR) photometry is needed. The combination of visible absolute magnitude and mid-IR derived radius permit a solution for the albedo, thus enabling the beaming parameter and thermophysical properties of the asteroid to be further constrained.

3.3. Lightcurve and shape

Visible wavelength lightcurves of 956 Elisa were measured to constrain its absolute magnitude, its rotational phase at the time of the Spitzer observations, and a first order estimation of its shape. These measurements were obtained at two observatories: the University of Hawaii 2.2 m telescope and a 40 cm telescope at the Observatoire de la Côte d’Azur. The data from the Observatoire de la Côte d’Azur were generously provided by Matthieu Conjat and were obtained over the course of nine nights between 2008–June–28 and 2008–July–12. All of these images were obtained using a Johnson R-band filter. These data were presented and made available through the CdR online data base of asteroid lightcurves (http://obswww.unige.ch/~behrend/page_cou.html).

The UH 2.2 m observations were performed over the course of three nights from 2008–July–26 to 2008–July–29. Images were obtained using an SDSS- r filter. Reduction of these data followed standard IRAF procedures. The observing conditions on 2008–July–26 were photometric, which resulted in a mean error of 0.014 on the measured magnitudes for that night. Though the magnitudes measured on the non-photometric nights were calibrated,

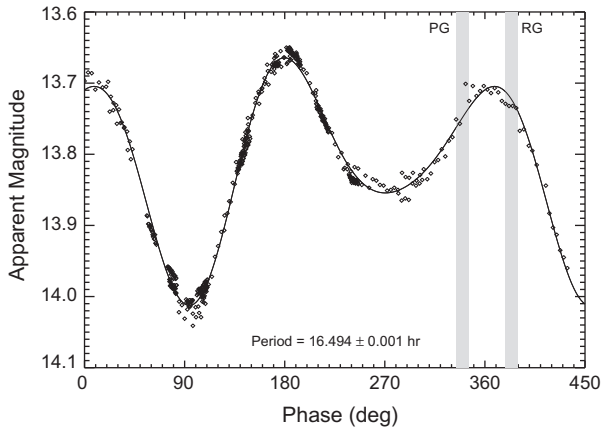


Fig. 3. Measured photometric lightcurve (in apparent SDSS-r band magnitude) of 956 Elisa. Data points from 12 separate nights of observations have been phase-folded onto a single period. The best fit lightcurve (solid line) displays a period of 16.494 ± 0.001 h and a peak-to-peak amplitude of 0.348 magnitude. The Spitzer observations viewed the asteroid at one of two possible rotational phases (shaded grey regions). These two possibilities (labeled PG for prograde rotation, and RG for retrograde rotation) exist due to the uncertainty in the orientation of Elisa's rotation axis.

we did allow a small additive offset to be applied to these data when determining the best fit lightcurve. Fig. 3 shows the phase folded lightcurve for 956 Elisa with data from all 12 nights of observations.

The measured magnitudes were fitted with a lightcurve of the form:

$$r(t) = \sum_{i=0}^3 a_i \sin\left(2\pi i \frac{t - \phi_{1i}}{P}\right) + b_i \cos\left(2\pi i \frac{t - \phi_{2i}}{P}\right) \quad (5)$$

where $r(t)$ is the r -band magnitude as a function of time. The coefficients (a_i, b_i), phases (ϕ_{1i}, ϕ_{2i}) and period (P) were treated as free parameters in the fitting algorithm. As mentioned above, small additive offsets were applied to the non-photometric data. Individual offsets were chosen for the set of data points from each night. These offsets were treated as free parameters and were restricted to within the photometric error bars. The best fit lightcurve was determined based on a minimization of the reduced chi-squared statistic. The fitted rotation period of the asteroid, P , was determined to be 16.494 ± 0.001 h. The high precision in this measurement was facilitated by an observational baseline of more than a month and resulted in rotational phase errors at the time of the Spitzer observations that were insignificant ($< 1^\circ$).

The orbital phase angle of Elisa (defined as the Sun-Elisa-observer angle) as seen by the Earth-trailing Spitzer observatory was different from the orbital phase as viewed from Earth. The Earth-based light curves were measured at an orbital phase of $\sim 7^\circ$ whereas Spitzer viewed Elisa at a phase angle of 29.3° . This difference results in a degeneracy in the assumed *rotational phase* observed by Spitzer. This degeneracy is caused by the unconstrained orientation of Elisa's spin axis. If Elisa rotates in a prograde sense then Spitzer saw the surface of Elisa associated with a rotational phase of $\sim 340^\circ$. If Elisa's rotation is retrograde, Spitzer saw the surface of Elisa associated with a rotational phase of $\sim 25^\circ$ (shown as $\sim 385^\circ$ in Fig. 3). This degeneracy can not be broken without knowledge of the orientation of Elisa's spin axis. Fortunately, the difference in magnitudes corresponding to these two rotational phases is small (Fig. 3).

In the prograde case, Spitzer observed Elisa at an apparent magnitude of $r = 13.75$; in the retrograde case, Spitzer observed at an apparent magnitude of $r = 13.73$. (Note that these are apparent

magnitudes as viewed from the Earth, not from Spitzer). From Eqs. (9) and (11) in Ivezić et al. (2001) we can calculate the absolute, phase corrected magnitudes of Elisa corresponding to these apparent values. These magnitudes are $H_r = 12.29$ (prograde) and $H_r = 12.27$ (retrograde). Converting this to V-band absolute magnitudes requires the assumption of a $g - r$ color for Elisa and a transform equation. The mean $g - r$ color of V-type asteroids is 0.24 (Moskovitz et al., 2008). Transform equations can be found in Smith et al. (2002) to give phase corrected absolute magnitudes of $H_V = 12.59$ (prograde) and $H_V = 12.57$ (retrograde) for Elisa at the time of the Spitzer observations. An average of these absolute magnitudes was used in the calculation of Elisa's albedo (Section 4).

The uncertainties associated with these absolute magnitudes are dominated by the the assumed $g - r$ color for Elisa. We estimate that this uncertainty is ± 0.04 based on the dispersion of $g - r$ colors amongst asteroids in the Vesta family (Moskovitz et al., 2008). There may also be uncertainties introduced by the use of a phase correction equation that was derived for S-type asteroids (Ivezić et al., 2001). Phase correction equations do not exist for V-type asteroids.

The amplitude of the lightcurve allows an estimation for the axial ratio of Elisa. This is achieved by assuming a tri-axial ellipsoid and a spin axis aligned perpendicular to the line of sight. Employing Eq. (1) from Masiero et al. (2009) and a measured peak-to-peak light curve amplitude of 0.35, we estimate Elisa is elongated with an axis ratio of at least 1.38.

3.4. Effects of shape on derived size and temperature

The thermal models used above to derive the size and temperature of Elisa assume a spherical shape, but the lightcurve (Fig. 3) demonstrates that this asteroid is not a perfect sphere. Departures from spherical shape change the surface temperature distribution due to different orientations of surface facets relative to the Sun, which can affect the radius derived assuming spherical shape. We fit the thermal flux spectrum of Elisa with an "ellipsoidal STM", assuming axial ratios $a:b:c$ of 1.38:1:1 inferred from the lightcurve and the possible rotational phases highlighted in Fig. 3. This model makes the same assumptions as the STM, except that the temperature solution and integration of flux are for a tri-axial ellipsoid rather than a sphere (e.g., Brown, 1985, though our implementation using matrix algebra eliminates the need for much of the tedious algebra described therein). The resulting best-fit *effective* radius (radius of a sphere with the same projected area as the ellipsoid) and sub-solar temperatures were well within the uncertainties quoted above for the spherical model ($\Delta r_{\text{eff}} < 0.1$ km and $\Delta T_{\text{max}} < 0.5$ K).

We note that the H magnitude at lightcurve mean is slightly lower than the H magnitude at the rotational phase of the Spitzer observations. Thus, our radius estimate of 5.3 ± 0.4 km at the time of the observation corresponds to a radius of 5.2 ± 0.4 km at lightcurve mean.

4. Albedo and thermal inertia

Combining the thermal results with the results of visible photometry enables us to solve for the albedo of the asteroid:

$$p_v = \frac{D_0^2}{(D^2)(10^{0.4H_v})} \quad (6)$$

Using the phase corrected absolute magnitude H_v from the lightcurve results in Section 3.3: $H_v = 12.58 \pm 0.04$, $D_0 = 1329.1 \pm 10.4$ km (Campins et al., 1985), and $D = 2R = 2(5.3 \pm 0.4$ km) [Section 3.1, above], we find that the geometric albedo of 956 Elisa is

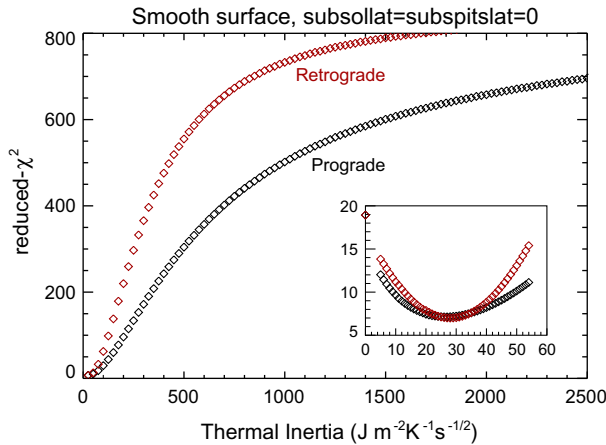


Fig. 4. Smooth-surface thermophysical models of 956 Elisa with equatorial viewing geometry. χ^2 of the best fit to the IRS spectrum of 956 Elisa vs. thermal inertia. The best-fit models are $20\text{--}30 \text{ J m}^{-2} \text{ K}^{-1} \text{ s}^{-1/2}$ in both the prograde and retrograde case.

$p_v = 0.142 \pm 0.022$. We note that this is significantly lower than the albedo of 4 Vesta (0.42 ± 0.05 ; Tedesco et al., 1992, 2002)² but comparable to that of the near-Earth basaltic Asteroid 3908 Nyx ($0.16^{+0.08}_{-0.05}$; Benner et al., 2002).

This albedo estimate may be applied to Eq. (4) by calculating the Bond albedo $A = qp_v$ (q is the phase integral (Bowell et al., 1989) assumed to be 0.39 ± 0.20 since no measurement is available), resulting in $\eta = 1.16 \pm 0.05$. This value is substantially higher than the $\eta \approx 0.756$ characteristic of large main-belt asteroids including 4 Vesta (Spencer, 1990; Lim et al., 2005).

Since 956 Elisa's rotation period is roughly three times as long as 4 Vesta's (16.49 h (above) vs. 5.342 h), if the surface layers of the two asteroids were identical in composition and structure the effect of thermal inertia would give Elisa the lower η value of the two. The thermal inertia of the surface layers of 956 Elisa must therefore be greater than that of Vesta's. We therefore conducted thermophysical modeling to quantify the constraints on 956 Elisa's thermal inertia.

4.1. Thermophysical modeling

Three sets of thermophysical models were calculated in order to constrain the thermal inertia of 956 Elisa's surface layers: a set of smooth-surface equatorial cases, a grid of smooth-surface cases with varying spin pole geometries, and a rough surface case.

The first thermophysical case, setting the minimum limit on thermal inertia, was calculated for a smooth asteroid surface with equatorial viewing geometry (sub-solar latitude = sub-Spitzer latitude = 0°). The IRS spectrum of 956 Elisa was then matched to thermophysical spectra calculated for a grid of thermal inertias from 5 to $2500 \text{ J m}^{-2} \text{ K}^{-1} \text{ s}^{-1/2}$ for both the prograde and retrograde senses of rotation (zero thermal inertia would correspond to the STM case); the asteroid's radius was allowed to float. The results are illustrated as Fig. 4. The best-fit thermal inertia solutions for this smooth-surface equatorial model are $25\text{--}30 \text{ J m}^{-2} \text{ K}^{-1} \text{ s}^{-1/2}$, corresponding to $T_{\max} = 289.2 \text{ K}$ for prograde rotation, and $T_{\max} = 289.4 \text{ K}$ for retrograde.

Since the spin pole of 956 Elisa is unknown, a similar calculation (with a coarser grid of thermal inertias) was then done over a set of 146 possible spin poles, at steps of 20° in ecliptic longitude and latitude. No solution produced a thermal inertia below the

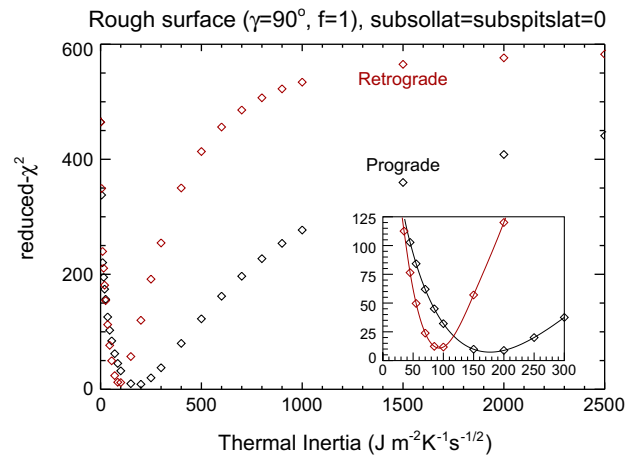


Fig. 5. A rough-surface thermophysical model of 956 Elisa. χ^2 is minimized for the rough-surface model at thermal inertia values of $175 \text{ J m}^{-2} \text{ K}^{-1} \text{ s}^{-1/2}$ (prograde) and $90 \text{ J m}^{-2} \text{ K}^{-1} \text{ s}^{-1/2}$ (retrograde).

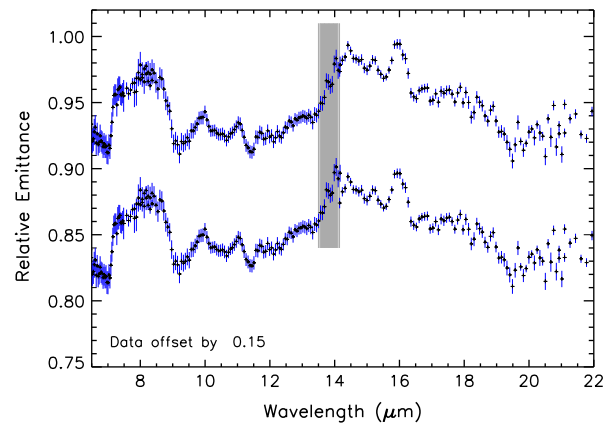


Fig. 6. Spitzer IRS spectrum of 956 Elisa in emissivity. The $13.5\text{--}14.15 \mu\text{m}$ region in the IRS, indicated by the grey box, is untrustworthy due to a sporadically appearing instrumental artifact [<http://ssc.spitzer.caltech.edu/irs/features.html>]. Upper trace: SL1/LL2 scaling of 0.84%, the result if the splice is performed with the unreliable “teardrop” region included. Lower trace: SL1/LL2 scaling of 2.57%, the result of excluding the “teardrop” region.

$20 \text{ J m}^{-2} \text{ K}^{-1} \text{ s}^{-1/2}$ established in the equatorial model, and nearly all fell between 20 and $100 \text{ J m}^{-2} \text{ K}^{-1} \text{ s}^{-1/2}$. The exception is the case of pole-on viewing geometry, in which a very high thermal inertia ($>2500 \text{ J m}^{-2} \text{ K}^{-1} \text{ s}^{-1/2}$, a value consistent with solid rock without a regolith cover) is possible, but such an observation is unlikely given the 0.4 mag. amplitude of the lightcurve. The distribution had T_{\max} between 284.3 and 292.2 K, consistent with the $282.3 \pm 2.8 \text{ K}$ derived from the simpler STM fitting.

Finally, a rough-surface thermophysical model with equatorial viewing geometry was calculated. To present the endmember case, 100% coverage by hemispherical craters was assumed, corresponding to RMS surface slope of 66° . Results are shown in Fig. 5. As expected, the best-fit thermal inertias are higher than in the smooth-surface case: 175 for prograde rotation, $90 \text{ J m}^{-2} \text{ K}^{-1} \text{ s}^{-1/2}$ for retrograde.

In summary, the IRS spectrum of 956 Elisa sets a firm lower limit of $20 \text{ J m}^{-2} \text{ K}^{-1} \text{ s}^{-1/2}$ for its surface layer. The most likely thermal inertia range is $30\text{--}150 \text{ J m}^{-2} \text{ K}^{-1} \text{ s}^{-1/2}$, consistent with unconsolidated sand or a mixture of rock and fine regolith. Knowledge of Elisa's spin pole and sense of rotation would significantly improve these estimates.

² A somewhat lower albedo for Vesta ($p_v \approx 0.35$) may be found using the size estimate from Thomas et al. (1997b) but this is still significantly higher than the albedo result for 956 Elisa.

Table 1

Sample numbers and size fractions of HED meteorite samples discussed in this work.

<i>Diogenites</i>			
Ellemeet (coarse)			RELAB MP-D2M-112
Ellemeet (fine)	0–25 μm		RELAB MP-D2M-113
LAP 91900, 29	0–1000 μm		RELAB TB-RPB-018
Johnstown	0–25 μm		RELAB MB-TXH-095-A
Johnstown (Salisbury et al., 1991)	0–75 μm		Johnstoft.txt
ALH 77256.96 (Salisbury et al., 1991)	0–75 μm		A77256f.txt
<i>Eucrites</i>			
ALHA 76005	Basaltic eucrite	0–1000 μm	RELAB TB-RPB-023
EET 90020	Basaltic eucrite	0–1000 μm	RELAB TB-RPB-020
PCA 82501	Basaltic eucrite	0–125 μm	RELAB MP-TXH-124
ALH 85001	Cumulate eucrite	0–1000 μm	RELAB TB-RPB-015
Yamato 980318	Cumulate eucrite (whole rock)	0–75 μm	RELAB MT-CMP-061
Yamato 980318	Plag. sep.	0–75 μm	RELAB MT-CMP-062
Yamato 980318	Px. sep.	75–150 μm	RELAB MT-CMP-063–064

Table 2

Synthetic and natural pyroxene samples in Fig. 11.

Synthetic pyroxenes (RELAB; Klima et al., 2005; Turnock et al., 1973)		
RELAB sample number	Pyroxene composition	
DL-CMP-001	En ₁₀₀	
DL-CMP-002	En ₈₀ Fs ₂₀	
DL-CMP-003	En ₇₅ Fs ₅₀	
DL-CMP-004	En ₅₀ Fs ₅₀	
DL-CMP-006	En ₂₅ Fs ₇₅	
DL-CMP-009	Wo ₁₀ En ₄₅ Fs ₄₅	
DL-CMP-010	Wo ₁₀ En ₆₃ Fs ₂₇	
DL-CMP-012	Wo ₅ En _{47.5} Fs _{47.5}	
DL-CMP-013	Wo ₈ En ₄₆ Fs ₄₆	
DL-CMP-016	Wo ₅ En ₇₆ Fs ₁₉	
DL-CMP-018-A	Wo ₁₀ En ₇₂ Fs ₁₈	
DL-CMP-019-A	Wo ₂₀ En ₅₆ Fs ₂₄	
DL-CMP-021-A	En ₈ Fs ₉₂	
DL-CMP-022-A	En ₇₅ Fs ₂₅	
DL-CMP-025-A	En ₃₅ Fs ₆₅	
DL-CMP-026-A	En ₇₀ Fs ₃₀	
DL-CMP-038-A	Wo ₉ En ₉₂	
DL-CMP-045-A	Wo ₄ En ₄₈ Fs ₄₈	
ASU pyroxenes (Hamilton, 2000)		
Sample number	ASU spectrum	Pyroxene composition
BUR-1920	439	Wo _{1.5} En ₇₇ Fs ₂₁
NMNH-166555	541	Wo _{0.5} En ₇₇ Fs ₂₂
NMNH-C2368	549	Wo _{4.2} En ₇₂ Fs ₂₄
NMNH-120414-1	552	Wo _{1.5} En ₇₅ Fs ₂₂
NMNH-93527	558	Wo ₃ En ₇₇ Fs ₂₂

5. Spectral features in the mid-IR

In the mid-IR, dividing the spectrum by the thermal continuum model yields the spectral emissivity variation of the asteroid (Fig. 6) which can then be used to constrain the surface mineralogy through comparison with spectra of laboratory samples, including HED meteorites, such as are available in the RELAB database (<http://www.planetary.brown.edu/rehab/>) and in Salisbury et al. (1991). A list of samples is given in Table 1.

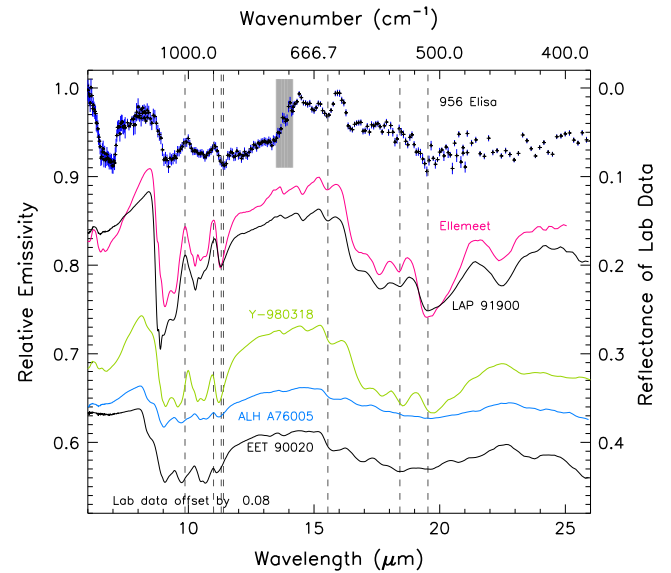


Fig. 7. Spitzer IRS spectrum of 956 Elisa in emissivity, with laboratory spectra (RELAB) of diogenites Ellemeet and LAP 91900, cumulate eucrite Y-980318, and basaltic eucrites ALHA 76005 and EET 90020. As in Fig. 6, the grey box represents the unreliable 13.5–14.15 μm “teardrop” region of the SL1 order of the IRS. Vertical dashed lines mark the locations of prominent spectral features discussed in the text, such as the “CA4” (11.4 μm) and “CA7” (19.5 μm) of Hamilton (2000).

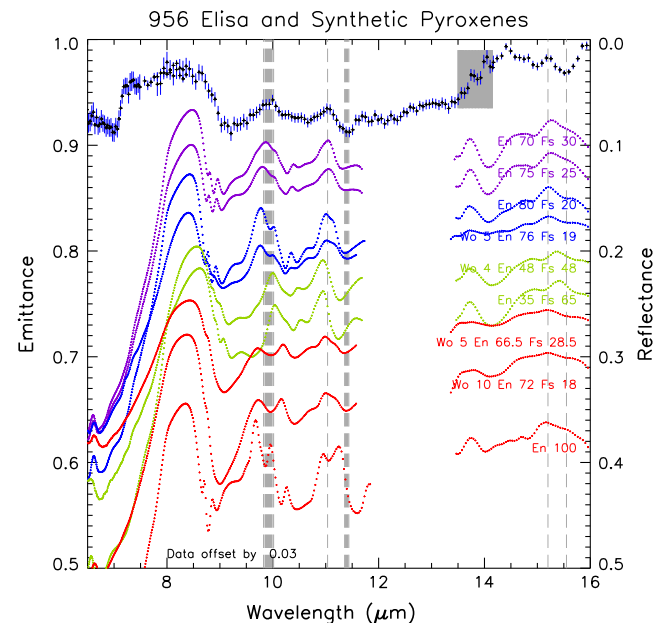


Fig. 8. Spectra of 956 Elisa and selected synthetic pyroxene samples plotted in Fig. 11. The 13.5–14.15 μm region in the IRS, indicated by the grey box, is untrustworthy due to an instrumental artifact (Section 3.2) and the transparency region (12–13.5 μm ; Section 5.1.1) has here been omitted from the laboratory spectra for clarity. Vertical dashed lines represent the wavelengths of various spectral features. For the 10 μm maximum and the 11.4 μm minimum (“CA4”), the widths of the lines indicate the formal uncertainties in the central positions from Gaussian fits to the spectrum of 956 Elisa. Sample numbers for the pyroxenes are given in Table 2.

Comparison with the spectra of HED meteorites (Fig. 7) reveals that the closest spectral matches to 956 Elisa are found among the diogenites. Like the laboratory spectra of diogenites, the spectrum of 956 Elisa exhibits two narrow maxima (10 μm , 11 μm) within the broad 9–14 μm silicate band, two maxima at 15.2 μm and 15.9 μm divided by a 15.55 μm minimum, a minimum in the

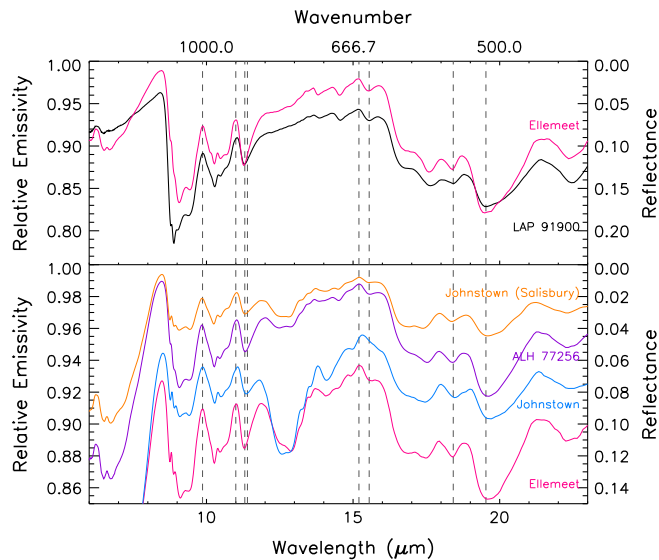


Fig. 9. Laboratory spectra of coarse and finely-particulate diogenite samples. See Table 1 for detailed sample identification. Top: RELAB spectra of coarse-grained samples from the diogenites Ellemeet (magenta) and LAP 91900 (black). The latter is labeled as a 0 to 1000 μm size fraction. Bottom: Spectra of finely particulate samples from three diogenites measured by RELAB and Salisbury et al. (1991): Ellemeet (purple; Salisbury et al., 1991), Johnstown (independent measurements by RELAB and Salisbury et al. (1991)), and ALH 77256 (Salisbury et al., 1991). RELAB sample numbers MP-D2M-113 and MB-TXH-095-A. The two RELAB samples are labeled as 0–25 μm size fractions; the two from Salisbury et al. (1991) are described as 0–75 μm particle size. Spectral contrast in the Salisbury et al. (1991) samples, taken on a biconical reflectance apparatus, has been scaled up by a factor of two to enable plotting on the same axes as the RELAB spectra. RELAB spectra have been offset for clarity. Note the reduced spectral contrast and the 12–13.5 μm transparency features appearing only in the spectra of the fine particle size samples. However, the wavelength positions of the reststrahlen features remain unchanged. (For interpretation of the references to colour in this figure legend, the reader is referred to the web version of this article.)

19–20 μm region, and a Christiansen feature (emissivity maximum) just shortward of 9 μm . We discuss these features in more detail below, beginning with the 9–14 μm reststrahlen features.

5.1. Spectral features in the 9–14 μm reststrahlen band

Spectral structure within the 9–14 μm reststrahlen band is a close match to that found in laboratory spectra of diogenites. In particular, the maxima at 10 and 11 μm and the minimum at 11.4 μm are narrow, distinct structures that closely match the diogenite spectra in wavelength.

The diogenites are dominated (>84% by volume) by orthopyroxene of a single very uniform major-element composition ($\text{Wo}_{2\pm 1}\text{En}_{74\pm 2}\text{Fs}_{24\pm 1}$; Mittlefehldt et al., 1998; although a few outliers extend the Mg range in known diogenitic orthopyroxenes to $\text{En}_{83.8}$ and $\text{En}_{66.4}$ (Mittlefehldt et al., 2009)). We examined the spectra of pyroxenes of a range of compositions in order to determine how sensitive the spectral features common to diogenites and to 956 Elisa are to pyroxene composition.

The 10- and 11- μm reststrahlen structures vary in shape and wavelength with pyroxene composition (Hamilton, 2000). The 10 μm emissivity maximum is bounded by the minima designated “critical absorptions” CA1 and CA2 by Hamilton (2000). Although Hamilton (2000) established the systematic variation of the wavelengths of CA1 and CA2 minima themselves with Fe content, we found it impractical to rely on our ability to determine the wavelengths of these minima in the spectrum of 956 Elisa. The short-wavelength side of CA1 is governed by the Christiansen feature, which may be shifted in wavelength by non-pyroxene minerals

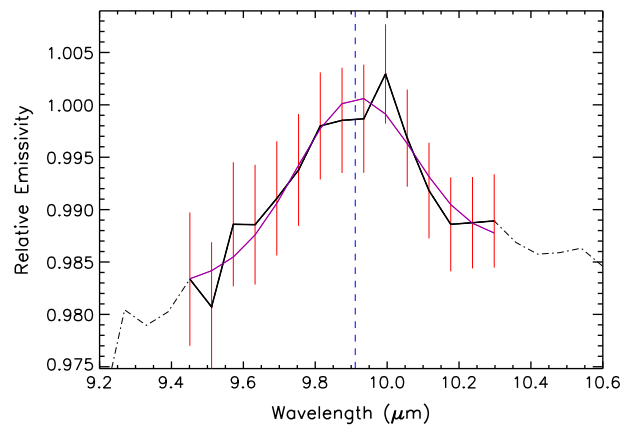


Fig. 10. Gaussian fit to the 10- μm structure in the emittance spectrum of 956 Elisa. The model (magenta trace) is a Gaussian with a linear background; the data are represented by the black trace with red error bars. The best-fit Gaussian is centered at $9.91 \pm 0.05 \mu\text{m}$. The same model applied to six available diogenite spectra resulted in an average Gaussian center of $9.85 \pm 0.01 \mu\text{m}$. (For interpretation of the references to colour in this figure legend, the reader is referred to the web version of this article.)

in the rock (for example, olivine) or by pressure and temperature effects (Logan et al., 1973). CA2 presented a different problem: at the S/N level of the Spitzer data, CA2 and CA3 are not readily distinguishable. For these reasons, we instead examined the wavelength of the 10 μm emissivity maximum, which also varies systematically with the Fe content of low-Ca pyroxenes and was readily identifiable in the Elisa data.

An upper limit on the Mg content of Elisa’s pyroxene may be set by the absence of the a local minimum at 9.9 μm that divides the 10 μm structure in magnesian orthopyroxenes En_{83} and above (Hamilton, 2000). This also eliminates less magnesian pyroxene compositions with $\text{Wo} > 5\%$ (Fig. 8). The six available mid-IR laboratory spectra of diogenites (Fig. 9) also lack this 9.9 μm minimum; the wavelength of the single local maximum in this region falls within a narrow range between 9.856 and 9.893 μm irrespective of particle size.

In order to determine the central wavelength and uncertainty of this 10 μm structure in the IRS spectrum of 956 Elisa, we applied a simple fit consisting of a Gaussian peak on a linear background to both the 956 Elisa spectra and the available diogenite laboratory spectra (ALH A77256, LAP 91900, Johnstown, and coarse and fine samples from Ellemeet) from 9.4 to 10.3 μm . The best-fit Gaussians for the meteorite spectra are centered around $9.85 \pm 0.01 \mu\text{m}$; the best fit to the spectrum of Elisa is $9.91 \pm 0.05 \mu\text{m}$ (Fig. 10). The width of the best Gaussian fit to the Elisa data is also consistent with the fits to the lab data: $0.16 \pm 0.07 \mu\text{m}$ for the asteroid vs. $0.20 \pm 0.02 \mu\text{m}$ among the laboratory spectra. (The uncertainties represent the formal uncertainties from the Gaussian fitting.) A similar Gaussian model was used to determine the position and uncertainty of the 11.4 μm minimum, the “CA4” of Hamilton (2000).

Fig. 11 shows the resulting positions for the 10 μm emissivity maxima vs. 11.4 μm minima in the spectra of 956 Elisa and various HED meteorites. The ellipses surrounding the points representing the diogenites and the basaltic and cumulate eucrites are 2σ from their respective means. For comparison, on the same figure, we have plotted the positions of these two features in the RELAB spectra of a collection of synthetic pyroxenes representing a range of compositions (Klima et al., 2005; Turnock et al., 1973) and ASU emissivity spectra of natural pyroxenes of near-diogenitic composition (Hamilton, 2000; Christensen et al., 2000). Diogenites and pyroxenes with diogenite-like compositions fall within 2σ of 956 Elisa, whereas more ferroan, more magnesian, and more calcic

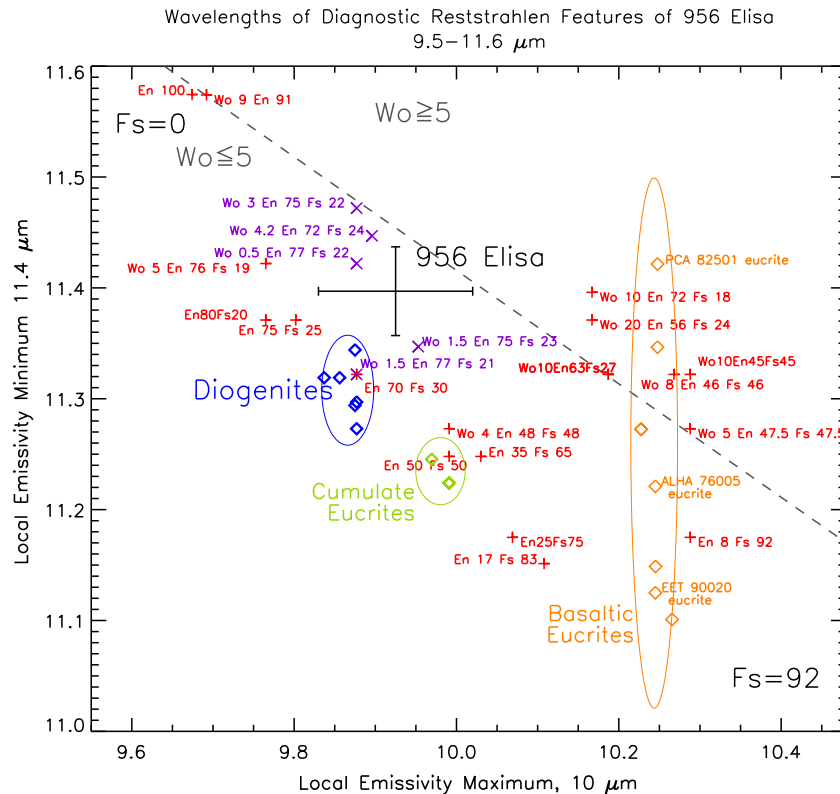


Fig. 11. Wavelengths of the 11.4 μm minimum (“CA4” of Hamilton (2000)) vs. the 10 μm maximum in the emissivity spectra of 956 Elisa, and natural pyroxenes of diogenite-like composition (purple) from the ASU collection described by Hamilton (2000). Also plotted are the same features as they appear in the inverted reflectance spectra of the synthetic pyroxenes (red) of Linsley and Turnock (RELAB; Klima et al., 2005, 1973) and of HED meteorites (shown as diamonds; RELAB and Salisbury et al. (1991)). Diogenites and pyroxenes with diogenite-like compositions plot within 2σ of 956 Elisa, whereas more ferroan, more magnesian, and more calcic pyroxenes plot outside this range. See Fig. 12. The plotted uncertainties in the location of Elisa’s features are the 1σ uncertainties emerging from a simple Gaussian fit to each feature (Fig. 10). (For interpretation of the references to colour in this figure legend, the reader is referred to the web version of this article.)

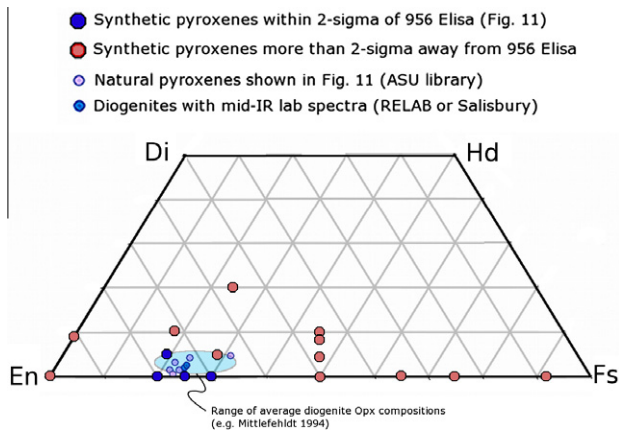


Fig. 12. Pyroxene quadrilateral illustrating the compositions of diogenites and pyroxene samples plotted in Fig. 11.

pyroxenes plot outside this range. We find that the wavelength of the CA4 minimum is negatively correlated with Fe content in the synthetic pyroxene spectra from En_{100} to En_{17} . The compositions of the pyroxenes represented on this figure are also plotted on the pyroxene quadrilateral in Fig. 12 and their spectra in Fig. 8.

Pyroxenes in the eucrites are significantly more ferroan than diogenitic pyroxenes; consequently, the cumulate eucrites plot below and to the right of 956 Elisa and the diogenite range on Fig. 11. Among the eucrites, basaltic eucrite pyroxenes are more ferroan than those of the cumulate eucrites. In Fig. 11, the basaltic eucrites consistently appear to the right (longer 10 μm peak) of the cumu-

late eucrites, but exhibit a wide range of CA4 wavelengths due to the broader widths of the CA4 minima in many of the basaltic eucrite spectra.

Unlike diogenites, eucrites contain substantial amounts of plagioclase feldspar in addition to their pyroxenes. We were able to evaluate the effect of plagioclase on the 10 μm and 11.4 μm pyroxene features in the spectrum of the cumulate eucrite Y-980318, for which spectra of both the whole rock and mineral separates (plagioclase and two pyroxenes) have been made available in the RELAB database (Pieters et al., 2006). The dominant pyroxene in Y-980318 is $\text{Wo}_{2.0}\text{En}_{51.9}$ (Buchanan and Tomiyama, 2003), consistent with the eucrite’s position in Fig. 11 near the synthetic $\text{En}_{50}\text{Fs}_{50}$ sample. Notably, the low-Ca pyroxene separates and the whole-rock mid-IR spectra have identical wavelength positions for both the 10 μm maximum and the 11.4 μm minimum, suggesting that these two spectral features are sensitive to pyroxene composition at the plagioclase abundances found in cumulate eucrites.

Thus, we find that the wavelength positions of the 10 μm maximum and the CA4 11.4 μm minimum are diagnostic of pyroxene composition, and that in this wavelength region the spectrum of 956 Elisa is more consistent with a diogenitic ($\text{Wo}_{2\pm 1}\text{En}_{74\pm 2}\text{Fs}_{24\pm 1}$) pyroxene composition than with other HED pyroxenes.

5.1.1. Transparency feature

We have not considered the 12–14 μm region in our compositional mixing models due to the strong effects of particle size in this region. Laboratory spectra of fine-grained silicate samples exhibit a minimum in emittance, known as the “transparency feature,” around 12 μm which is absent from the spectra of coarse-grained samples (see for example Fig. 9). This feature is also

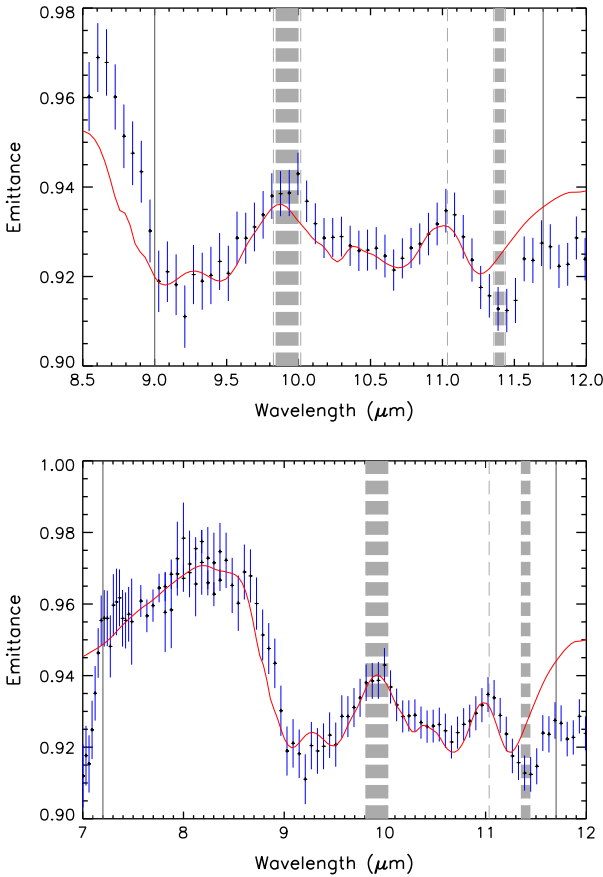


Fig. 13. Linear mixing models of the spectrum of 956 Elisa. Vertical dashed bars mark the locations of the 10 μm emissivity maximum, the 11 μm maximum, and CA4 in the spectrum of Elisa. Top: The first fit considered only the reststrahlen features (from 9.0 to 11.7 μm) and resulted in a mixture of approximately 85% Ellemeet diogenite and 15% olivine (excluding the spectrally neutral component; see Table 3). Bottom: Fitting region from 7.2 to 11.7 μm , including the Christiansen feature. The best fit with the Christiansen feature included 40% Ellemeet diogenite, 35% cumulate eucrite, 12% olivine, and 12% basaltic eucrite, again excluding a neutral component.

absent from the IRS spectrum of 956 Elisa, which may suggest a relatively coarse particle size.

However, caution is required when interpreting the transparency feature on airless bodies as the feature may behave differently under vacuum than when measured at atmospheric pressure in the laboratory. Henderson et al. (1996) presented emissivity spectra of 50 μm quartz particles measured in an environment chamber at different pressures. A transparency feature between 10 and 12 μm that is present under higher pressure is absent in the spectrum measured under near-vacuum (10^{-3} Torr). Unfortunately, in the pioneering study of the effects of pressure on emission spectra, Logan et al. (1973) did not measure the transparency region of their granite samples. Model calculations by Henderson and Jakosky (1997) for both quartz and basalt reproduce their earlier measurements, showing a decrease in contrast of the transparency feature with decreasing pressure. However, their work indicates that the effects of particle size on the transparency feature are far more dramatic than the effects of vacuum. The absence of a transparency feature in the mid-IR spectrum of Elisa is therefore likely to indicate a fairly coarse-grained regolith, but this conclusion cannot be confirmed without further laboratory data.

5.1.2. Linear mixing models

In order to investigate the presence and abundance of additional mineralogical components such as plagioclase, olivine, and

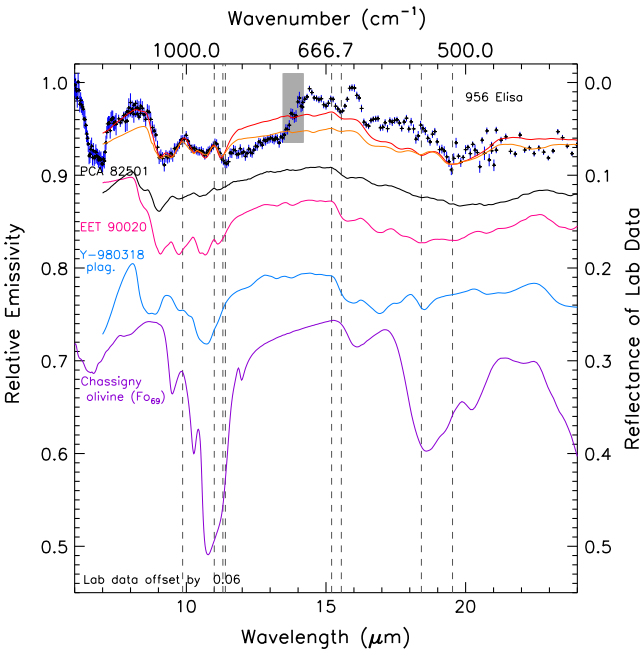


Fig. 14. Linear mixing models from Fig. 13 and endmembers with the spectrum of 956 Elisa. Spectra of other endmembers, such as Ellemeet, LAP 91900, Y-980318, and ALH A76005 may be found in Figs. 7 and 9.

Table 3
Results of linear mixing models.

Component	Type	Wavelength range	
		9–11.7 μm	7.2–11.7 μm
Ellemeet (coarse)	Diogenite	0.22	0.20
Ellemeet (fine)	Diogenite	—	—
LAP 91900	Diogenite	—	—
Chassigny olivine	Fo 69	0.04	0.06
Y-980310 whole-rock	Cumulate eucrite	—	0.17
Y-980310 plagioclase	An 88–91	—	—
Y-980318 Fe–Px	Wo 2 Fs 48–49	—	—
Y-980318 Ca–Px	Wo 45–46 Fs 18–19	—	—
EET 90020	Basaltic eucrite	—	0.06
ALH A76005, PCA 82501	Basaltic eucrites	—	—
Spectrally neutral		0.74	0.51

additional HED materials, we applied a linear mixing model to the 7–12 μm region of the Spitzer spectrum of 956 Elisa. As endmembers, we used three diogenite spectra, three basaltic eucrite spectra, the whole-rock spectrum of the cumulate eucrite Y-980318, plagioclase (An_{88–91}) and pyroxene separates from Y-980318, and a spectrum of a Chassigny olivine sample Fo₆₉, representing the olivine composition found in diogenites (Mittlefehldt, 1994) and in the HED-related dunite MIL 03443 (Mittlefehldt, 2008), Fo₆₅–Fo₇₆. Although RELAB spectra, which are measured in reflectance at terrestrial atmospheric pressure, are not ideal for permitting rigorous quantitative deconvolution of thermal emission spectra, these currently represent the best available spectra of samples of the appropriate particle sizes for the regolith of 956 Elisa. Thus, deconvolution against these spectra provides a useful qualitative check on which components are most likely to be present and a rough estimate of their relative abundances.

Models of the Christiansen feature (<9 μm emissivity maximum) using spectral endmembers measured under atmospheric pressure must be interpreted with caution. The few mid-IR spectroscopy studies conducted under vacuum (Logan et al., 1973; Henderson et al., 1996) have found that the Christiansen feature migrates in wavelength at very low pressures (see also Henderson

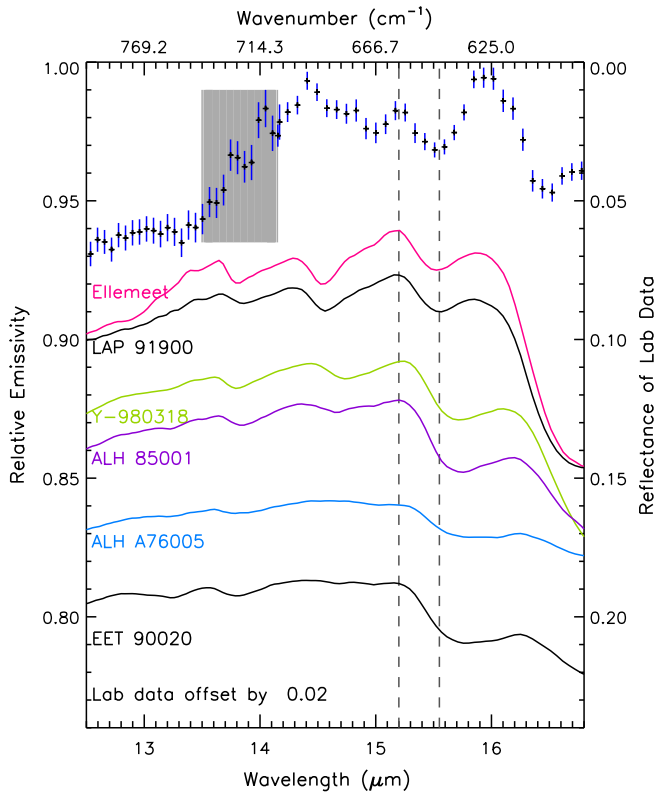


Fig. 15. Spectrum of 956 Elisa from 12.5 to 16.8 μm . As in Fig. 7, the 13.5–14.15 μm region in the spectrum of Elisa is marked by a grey box to indicate the unreliability of the IRS in this range. Also shown are the RELAB spectra of two diogenites (Ellemeet and LAP 91900), two cumulate eucrites (Y-980318 and ALH 85001), and two basaltic eucrites (ALH A76005 and EET 90020). The wavelengths of the 15.2 μm maximum and 15.55 μm minimum (marked by vertical dashed lines) are a close match in the spectra of Elisa and the two diogenites.

and Jakosky (1997) in which basalt features were modeled but not measured). However, since the experiments both involved very silic samples (granite and quartz powders), we cannot confidently quantify the direction or degree of wavelength change of the Christiansen feature of any mafic mineral under vacuum.

We therefore considered two wavelength ranges: 9.0–11.7 μm , which isolates the reststrahlen features from the Christiansen and transparency regions; and 7.2–11.7 μm , which includes the Christiansen feature. Figs. 13 and 14 illustrate the results of the linear mixing models; coefficients are given in Table 3.

When only the reststrahlen features are considered, the best fit is given by a combination of the Ellemeet diogenite spectrum at coarse (0–1 mm) particle size and olivine, with the diogenite approximately five times as abundant as the olivine. No other component improved the fit. This suggests an olivine diogenite composition for 956 Elisa.

However, when the Christiansen feature is included, the best fit includes two eucritic components: 40% Ellemeet diogenite, 35% cumulate eucrite, 12% olivine, and 12% basaltic eucrite, excluding a spectrally neutral component. This model achieves a good match to the Christiansen feature at the expense of the CA4 region (11.4 μm); every component in this mixture apart from the diogenite has the effect of shifting the model's CA4 minimum further shortward of the CA4 location in the asteroid spectrum. This problem is also present to a lesser degree in the reststrahlen-only fit, since the olivine in that case influences CA4 in the same way. Thus, although these models provide the best overall fits to their respective fitting regions, neither matches the CA4 feature as well as a single diogenite spectrum.

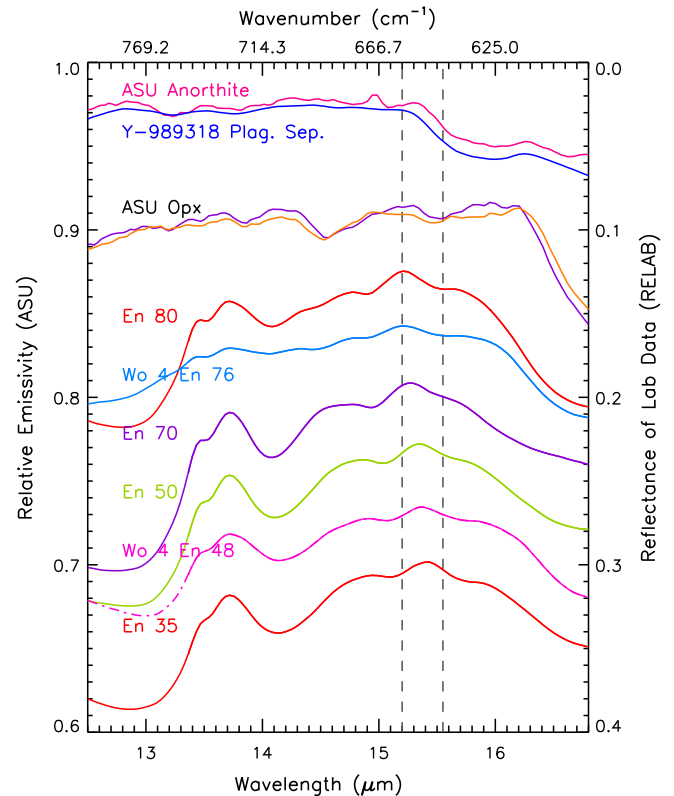


Fig. 16. Spectra of plagioclases and pyroxenes from 12.5 to 16.8 μm . Dash-dotted portions of the synthetic pyroxene spectra indicate the transparency feature, found only in spectra of finely particulate samples (hence absent here from the ASU spectra of similar mineralogy). The wavelengths of the 15.2 μm maximum and 15.55 μm minimum as found in the spectra of 956 Elisa and diogenites (Fig. 15) are marked by vertical dashed lines. The 15.55 μm minimum is a weak shoulder in the synthetic orthopyroxene spectra (six lower traces). However, the wavelength of the 15.2 μm maximum is evidently correlated with Mg/(Mg + Fe) composition. Spectra have been offset for clarity.

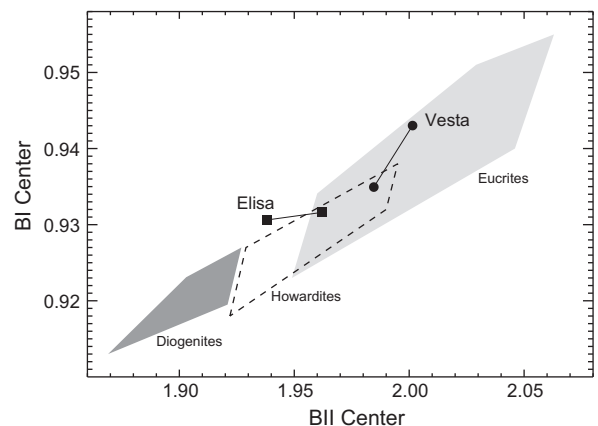


Fig. 17. NIR band centers of 956 Elisa compared with those of 4 Vesta and the HED meteorites. The errors on the band centers for the asteroids are comparable to the size of the plotted symbols. By direct comparison to the meteorites, the band centers of Elisa are most similar to the howardites.

Other components in the library (Table 3), including the LAP 91900 diogenite, were excluded from both fits. Ellemeet may provide a better match than LAP 91900 because of its greater olivine content; Ellemeet has 4.7% modal olivine, whereas LAP 91900 has under 1% (Bowman et al., 1997). Combining Ellemeet's olivine with the olivine from the Chassigny component in the linear mixture

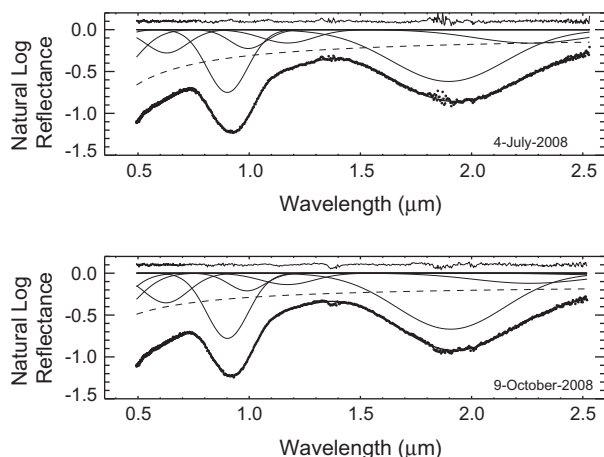


Fig. 18. Modified Gaussian Model (MGM) fits to the NIR spectrum of 956 Elisa. MGM band parameters are consistent with a composition for Elisa that is approximately 75% magnesian orthopyroxene (e.g. diogenite-like) and 25% high-Ca pyroxene. The average HCP/(HCP + LCP) value from the MGM fits is 26% with variation of order $\pm 5\%$.

raises the olivine proportions in the mixtures to 18% and 14% for the reststrahlen-only and Christiansen-feature models respectively.

Apart from the uncertainty in the behavior of the Christiansen feature itself under vacuum, another possible explanation for the compositional differences between the two regions is particle size: unlike that of the Christiansen feature, the spectral contrast of reststrahlen features is known to be reduced at fine particle sizes (e.g. Logan et al., 1973). Thus, the Christiansen feature is more likely to reflect the bulk composition of the material, whereas the reststrahlen features will strongly overrepresent the coarsest particulate material in the field of view.

5.2. Spectral features, 14–17 μm

Hamilton (2000) notes that features in the 800–600 cm^{-1} region (12.5–16.7 μm) are produced by symmetric Si–O–Si stretching vibrations and weaken in band strength with increasing Fe, but does not evaluate their diagnostic potential because of their low spectral contrast in the ASU library pyroxene samples.

However, the spectrum of 956 Elisa exhibits maxima at 15.2 and 15.9 μm , separated by a 15.55 μm emissivity minimum, that are closely matched in wavelength by the RELAB spectra of diogenites (Fig. 15). In cumulate eucrite spectra in this region a similar feature occurs at a slightly longer wavelength; in basaltic eucrite spectra the minimum is significantly weaker and occurs at a longer wavelength still.

In the RELAB spectra of synthetic low-Ca pyroxenes (Fig. 16), the wavelength of the 15.2 μm maximum is evidently correlated with En content. The wavelengths of this feature in the spectrum of the En_{80} and $\text{Wo}_{4}\text{En}_{76}$ samples are the closest matches to its wavelength in the diogenite spectra (and in the spectrum of 956 Elisa), a result consistent with the known diogenite pyroxene compositions.

We note that the two diogenite spectra in Fig. 15 also display a narrow minimum at 14.6 μm which is not evident in the spectrum of 956 Elisa; however, it is also absent from spectra of several of the finely-particulate diogenite samples (Fig. 9).

5.3. 16–25 μm reststrahlen features

Four “critical absorptions” were identified in orthopyroxenes by Hamilton (2000) in the 16–25 μm reststrahlen region at 17.6, 18.4, 19.5, and 22.1 μm , with the observation that none of them deviates

Table 4
MGM band parameters.

	Center (μm)	Width (μm)	Strength (log reflectance)
4-July-2008			
Band 1	0.277	0.223	−0.40
Band 2	0.376	0.264	−0.57
Band 3	0.629	0.219	−0.28
Band 4	0.902	0.216	−0.75
Band 5	0.995	0.189	−0.23
Band 6	1.173	0.277	−0.16
Band 7	1.897	0.602	−0.62
Band 8	2.268	0.587	−0.16
Band 9	2.600	0.505	−8E−4
Continuum intercept = 0.945, slope = $-0.021 \mu\text{m}^{-1}$			
Residual = 1.20%			
8-October-2008			
Band 1	0.280	0.289	−0.74
Band 2	0.374	0.278	−0.52
Band 3	0.626	0.237	−0.36
Band 4	0.902	0.219	−0.78
Band 5	0.990	0.190	−0.21
Band 6	1.172	0.282	−0.14
Band 7	1.906	0.573	−0.67
Band 8	2.262	0.590	−0.12
Band 9	2.603	0.516	−0.02
Continuum intercept = 0.882, slope = $-0.013 \mu\text{m}^{-1}$			
Residual = 1.11%			

substantially in wavelength as a function of Mg or Fe content. Of these, only the deepest (CA7, 19.5 μm) is readily identifiable in the spectrum of 956 Elisa. CA7 is found at the same wavelength in the spectra of diogenites; at a lower spectral contrast and slightly longer wavelength in the spectra of cumulate eucrites; and not at all in the spectra of basaltic eucrites.

6. Near-IR spectroscopy

Near-infrared (NIR, 0.75–2.5 μm) spectra of 956 Elisa were obtained to complement the mid-IR Spitzer observations. Data were obtained on 4-July-2008 and 9-October-2008 at NASA’s Infrared Telescope Facility (IRTF) using the SpeX instrument (Rayner et al., 2003). Reduction of these data employed the IDL-based Spextool package (Cushing et al., 2004). Since these data did not display significant spectral variability as a function of Elisa’s rotational phase (the longest base line that was tested was ~ 3 h on 9-October-2008), we combined individual exposures from each night into two final spectra. The maximum time for individual exposures was 120 s and the net exposure time for 4-July-2008 was 16 min and for 9-October-2008 was 88 min. Visible-wavelength data from Lazzaro et al. (2004) were appended to our NIR data to extend the spectral range down to 0.5 μm .

A simple band analysis in the style of Cloutis et al. (1986) was performed for each of the NIR spectra. Specific definitions of the band parameters measured here can be found in Moskovitz et al. (2010). The temperature-corrected (Burbine et al., 2009) 1 and 2 μm (BI and BII respectively) band centers were measured at 0.932 and 1.962 μm for the data from 4-July-2008 and at 0.931 and 1.938 μm for the data from 9-October-2008.

The temperature corrections were calculated using the measured albedo of 0.142 (Section 4) and were found to be 0.002 μm for BI and 0.017 μm for BII. These corrections are the same for both nights because the heliocentric distance of Elisa happened to be the same. The error bars on these band centers are no greater than 0.002 μm for BI and 0.01 for BII. These band centers are plotted in Fig. 17 along with those of asteroid 4 Vesta and the regions occupied by each of the HED meteorite subgroups (Moskovitz et al.,

2010). This figure shows that by spectral analogy the band centers of Elisa are most consistent with a howardite-like composition. However, it is important to note that these band centers represent a simplified parameterization of the 1 and 2 μm absorption features. In reality these features are produced by several overlapping bands, each with distinct central wavelengths. As a result the measured band centers merely provide approximate indications of bulk composition.

The measured band centers can be used with the equations of Gaffey et al. (2002) and Burbine et al. (2009) to compute bulk single-pyroxene Fs and Wo molar contents. As the difference in measured band centers from the two nights of observing are not significant in these calculations, average values are presented. The equations of Gaffey et al. (2002) predict $Fs = 40 \pm 5$ and $Wo = 9 \pm 4$. The equations of Burbine et al. (2009) predict values of $Fs = 38 \pm 3$ and $Wo = 8 \pm 1$. These Fs–Wo numbers suggest a pyroxene composition for Elisa that is consistent with polymict eucrites and howardites (Burbine et al., 2001, 2009).

These results merit further investigation, particularly in light of our mid-IR analysis (Section 5) which suggests a composition dominated by diogenite-like, low-Ca pyroxene (LCP). Thus, we employ the modified gaussian model (MGM; Sunshine et al., 1990) to provide a more realistic treatment of Elisa's NIR absorption features. Fig. 18 shows the results of this MGM analysis and Table 4 summarizes the parameters of the fitted bands. Following convention (e.g. Sunshine et al., 1990) the data have been renormalized so that the peak reflectance around 1.4 μm is less than unity, hence the negative values of $\ln(\text{reflectance})$ shown in Fig. 18. In short, we were unable to fit Elisa's NIR spectrum using only LCP: both LCP and HCP were required to produce a reasonable fit.

Nine bands were used to model the reflectance spectra of Elisa: three visible wavelength bands centered around 0.3, 0.4 and 0.6 μm , the primary LCP bands near 0.9 and 1.9 μm , the primary HCP bands near 1.0 and 2.2 μm , one band around 1.2 μm and an atmospheric water band around 2.6 μm . The modeling of pyroxene-dominated compositions with these nine bands is consistent with previous studies (Sunshine et al., 2004, Mayne et al., submitted for publication). The residual root-mean-square (RMS) errors on these fits were $\sim 1\%$.

The MGM bands display similar central wavelengths, widths and strengths in the two spectra. The variation that does exist (Table 4) is most likely a consequence of bands shifting to compensate for differences in the residual atmospheric features near 1.4 and 1.9 μm . Comparison of Elisa's LCP band centers (Bands 4 and 7 in Table 4) to those of synthetic pyroxenes (Klima et al., 2007) suggest a Mg# certainly greater than 50 and probably closer to ~ 80 . The ratio of LCP to HCP band strengths in both the 1 and 2 μm bands give an indication of the fraction of surface material composed of HCP (Sunshine and Pieters, 1993). The average $HCP/(HCP + LCP)$ value from the MGM fits is 26% with variation of order $\pm 5\%$.

In total, these MGM band parameters suggest a composition for Elisa that is approximately 75% magnesian orthopyroxene (e.g. diogenite-like) and 25% high-Ca pyroxene. This is consistent with the result of our simple band analysis (Fig. 17). The presence of high-Ca pyroxene pushes Elisa's BI and BII centers towards longer wavelengths than would be consistent with a composition of exclusively diogenite-like material. Considering that the band analysis performed for Fig. 17 provides a rough, first-order approximation of mineralogy, we feel that these two techniques provide complementary insight on the composition of Elisa.

7. Discussion and comparison with near-IR spectra

Based on the wavelengths of the 10 μm maximum, the 11.4 μm minimum, and the 15.2–15.9 μm Si–O–Si symmetric stretching

features, as well as the strength of the 19.5 μm minimum, we conclude that the Spitzer IRS spectrum of 956 Elisa is most consistent with thermal emission from a material of predominantly olivine-diogenitic composition. Non-cumulate (basaltic) eucrite spectra cannot account for the observed features. The general pattern of reststrahlen features in the cumulate eucrite spectra is similar to that found in diogenites and the IRS data, but the CA4 minimum (11.4 μm), 15.2–15.9 μm features, and CA7 minimum (19.5 μm) are all somewhat poorer matches to 956 Elisa in wavelength than are the diogenite equivalents. Comparison with the library suites of pyroxenes establishes that these small shifts in wavelength are compositionally meaningful.

High-Ca pyroxene is present at $25\% \pm 5\%$ in the MGM solution to the near-IR spectra. Two-pyroxene solutions to the spectra of Vestoids have been uncommon in the literature. This is a considerably lower level than the 59–66% found for the three V-type near-Earth asteroids (3908 Nyx, 4055 Magellan, and (6611) 1993 VW) by Canas et al. (2008), and slightly lower than the 30–40% found for 4188 Kitezh by Sunshine et al. (2004). Calcic pyroxene is not evident in the mid-IR spectrum of 956 Elisa, but may belong to a component that is underrepresented in the mid-IR spectrum either because of its spatial distribution on the asteroid or because of its particle size. In addition, high-Ca pyroxene may be present as exsolution lamellae: fine-scale exsolution has been found in some diogenites, and the natural orthopyroxene samples of Hamilton (2000) were sometimes noted to have included exsolution impurities that appeared not to have affected the mid-IR spectra. Thus, it is possible that exsolved pyroxenes may be less evident in thermal-IR spectra than they are in the near-IR.

Among HED materials, high-Ca pyroxene occurs in eucrites and is usually accompanied by plagioclase. Although various eucrites and a eucritic plagioclase were included in the spectral library for the fitting of the 9–11.7 μm reststrahlen features, the best fits to this region were plagioclase-free. In contrast, the fits to the Christiansen feature consistently produced compositions containing substantial amounts of eucritic material. This combination suggests a particle size effect: at small particle sizes, spectral contrast in the reststrahlen features is suppressed, but spectral contrast in the Christiansen feature is not.

The hypothesis that eucritic and diogenitic material on 956 Elisa occur at different particle sizes suffers from the obvious drawback that the two lithologies do not have very different mechanical properties. One possible solution is that a recent impact into a diogenitic terrane on Elisa may have excavated fresh orthopyroxenite.

Thermal infrared observations are also strongly biased toward the warmest part of the asteroid in comparison with near-IR observations. For example, 76% of the IRS flux would have originated within 50° of the sub-solar point, a region representing 37% of the visible hemisphere. Nevertheless, the IRS and SpeX observations are both consistent with the presence of a substantial amount of diogenitic pyroxene observable on 956 Elisa.

In summary, on the basis of Spitzer IRS data and new ground-based observations of 956 Elisa, we determine that the rotation period of 956 Elisa is 16.494 ± 0.001 h; that its geometric albedo is $p_v = 0.142 \pm 0.022$; that its radius is 5.3 ± 0.4 km; that its maximum surface temperature at the time of observation was 282.3 ± 2.8 K; and that its thermal spectrum is a good match to the standard thermal model with $\eta = 1.16 \pm 0.05$. Thermophysical modeling of the IRS spectrum of Elisa places a firm lower limit of $20 \text{ J m}^{-2} \text{ K}^{-1} \text{ s}^{-\frac{1}{2}}$ on the thermal inertia of the asteroid's surface layer (if the surface is very smooth) but more likely values fall between 30 and $150 \text{ J m}^{-2} \text{ K}^{-1} \text{ s}^{-\frac{1}{2}}$ depending on the sense of rotation, which remains unknown.

Spectral features observed within the 9–12 μm reststrahlen band, the 15–16.5 μm symmetric Si–O–Si region (Hamilton,

2000), and the 16–25 μm reststrahlen region are closely matched by features found in laboratory spectra of diogenite meteorites. Non-cumulate (basaltic) eucrite spectra cannot account for the features observed in the IRS spectrum of 956 Elisa; linear spectral deconvolution against a suite of HED meteorite spectra and related samples suggests that they can be excluded as a major component of the portion of 956 Elisa represented by the IRS spectrum. Cumulate eucrite material may be present at lower abundances than the diogenitic component. However, the diagnostic 9–12 μm reststrahlen features are better fit by a mixture of diogenite and 10–15% olivine (e.g. olivine diogenite) than by a mixture that includes cumulate eucrites.

Acknowledgments

This work is based in part on observations made with the Spitzer Space Telescope, which is operated by the Jet Propulsion Laboratory, California Institute of Technology under a contract with NASA. Support for this work was provided by NASA. N.M. acknowledges the support of NASA GSRP Grant NNX06AI30H, J.P.E. and L.L. were also supported in part by NASA PG&G Grant NNX08BA78G.

For the Mauna Kea NIR data, the authors are indebted to the indigenous people of Hawai'i. We also thank the IRTF staff for their contribution to the IRTF data obtained by N.M. as a Visiting Astronomer at the Infrared Telescope Facility. IRTF is operated by the University of Hawaii under Cooperative Agreement no. NNX-08AE38A with the National Aeronautics and Space Administration, Science Mission Directorate, Planetary Astronomy Program.

In addition, the authors would especially like to express their appreciation to Matthieu Conjat for providing lightcurve data; Beth Clark and Maureen Ockert-Bell for investigating rotational variability (or the lack thereof) in the NIR spectrum; Rhiannon Mayne for valuable assistance with the MGM and for sharing her pre-publication manuscript; Vicky Hamilton, the NASA RELAB facility at Brown University, and various RELAB investigators for the laboratory spectra used in this work (Tables 2 and 3); Vicky Hamilton (again), Hap McSween, and Jess Sunshine for useful discussions; and Rachel Klima and Marco Delbò for helpful reviews.

References

- Benner, L.A.M., Ostro, S.J., Hudson, R.S., Rosema, K.D., Jurgens, R.F., Yeomans, D.K., Campbell, D.B., Chandler, J.F., Shapiro, I.L., 2002. Radar observations of Asteroid 3908 Nyx. *Icarus* 158, 379–388.
- Binzel, R.P., Xu, S., 1993. Chips off of Asteroid 4 Vesta – Evidence for the parent body of basaltic achondrite meteorites. *Science* 260, 186–191.
- Binzel, R.P., Gaffey, M.J., Thomas, P.C., Zellner, B.H., Storrs, A.D., Wells, E.N., 1997. Geologic mapping of Vesta from 1994 Hubble Space Telescope images. *Icarus* 128, 95–103.
- Bowell, E., Hapke, B., Domingue, D., Lumme, K., Peltoniemi, J., Harris, A.W., 1989. Application of photometric models to asteroids. In: Binzel, R.P., Gehrels, T., Matthews, M.S. (Eds.), *Asteroids*, vol. II. pp. 524–556.
- Bowman, L.E., Spilde, M.N., Papike, J.J., 1997. Automated EDS modal analysis applied to the diogenites. *Meteorit. Planet. Sci.* 32, 869–875.
- Brown, R.H., 1985. Ellipsoidal geometry in asteroid thermal models – The standard radiometric model. *Icarus* 64, 53–63.
- Buchanan, P.C., Tomiyama, T., 2003. Thermal effects associated with the formation of cumulate eucrites, including Yamato 980318. *Meteorit. Planet. Sci. Suppl.* 38, 5064.
- Burbine, T.H., Buchanan, P.C., Binzel, R.P., Bus, S.J., Hiroi, T., Hinrichs, J.L., Meibom, A., McCoy, T.J., 2001. Vesta, vestoids, and the howardite, eucrite, diogenite group: Relationships and the origin of spectral differences. *Meteorit. Planet. Sci.* 36, 761–781.
- Burbine, T.H., Buchanan, P.C., Dolkar, T., Binzel, R.P., 2009. Pyroxene mineralogies of near-Earth vestoids. *Meteorit. Planet. Sci.* 44, 1331–1341.
- Campins, H., Rieke, G.H., Lebofsky, M.J., 1985. Absolute calibration of photometry at 1 through 5 microns. *Astron. J.* 90, 896–899.
- Canas, L., Duffard, R., Seixas, T., 2008. Mineralogy of HED meteorites using the modified Gaussian model. *Earth Moon Planets* 102, 543–548.
- Carruba, V., Michtchenko, T.A., Roig, F., Ferraz-Mello, S., Nesvorný, D., 2005. On the V-type asteroids outside the Vesta family. I. Interplay of nonlinear secular resonances and the Yarkovsky effect: The cases of 956 Elisa and 809 Lunda. *Astron. Astrophys.* 441, 819–829.
- Carruba, V., Roig, F., Michtchenko, T.A., Ferraz-Mello, S., Nesvorný, D., 2007. Modeling close encounters with massive asteroids: A Markovian approach. An application to the Vesta family. *Astron. Astrophys.* 465, 315–330.
- Christensen, P.R., Bandfield, J.L., Hamilton, V.E., Howard, D.A., Lane, M.D., Piatek, J.L., Ruff, S.W., Stefanov, W.L., 2000. A thermal emission spectral library of rock-forming minerals. *J. Geophys. Res.* 105, 9735–9740.
- Cloutis, E.A., Gaffey, M.J., Jackowski, T.L., Reed, K.L., 1986. Calibrations of phase abundance, composition, and particle size distribution for olivine-orthopyroxene mixtures from reflectance spectra. *J. Geophys. Res.* 91, 11641–11653.
- Consolmagno, G.J., Drake, M.J., 1977. Composition and evolution of the eucrite parent body – Evidence from rare Earth elements. *Geochim. Cosmochim. Acta* 41, 1271–1282.
- Cushing, M.C., Vacca, W.D., Rayner, J.T., 2004. Spextool: A spectral extraction package for SpeX, A 0.8–5.5 micron cross-dispersed spectrograph. In: *Publications of the Astronomical Society of the Pacific*, vol. 116. pp. 362–376.
- Duffard, R., Lazzaro, D., Licandro, J., de Sanctis, M.C., Capria, M.T., Carvano, J.M., 2004. Mineralogical characterization of some basaltic asteroids in the neighborhood of (4) Vesta: First results. *Icarus* 171, 120–132.
- Florczak, M., Lazzaro, D., Duffard, R., 2002. Discovering new V-type asteroids in the vicinity of 4 Vesta. *Icarus* 159, 178–182.
- Gaffey, M.J., 1997. Surface lithologic heterogeneity of Asteroid 4 Vesta. *Icarus* 127, 130–157.
- Gaffey, M.J., Cloutis, E.A., Kelley, M.S., Reed, K.L., 2002. Mineralogy of asteroids. In: *Asteroids III*, pp. 183–204.
- Hamilton, V.E., 2000. Thermal infrared emission spectroscopy of the pyroxene mineral series. *J. Geophys. Res.* 105, 9701–9716.
- Harris, A.W., 1998. A thermal model for near-Earth asteroids. *Icarus* 131, 291–301.
- Henderson, B.G., Jakosky, B.M., 1997. Near-surface thermal gradients and mid-IR emission spectra: A new model including scattering and application to real data. *J. Geophys. Res.* 102, 6567–6580.
- Henderson, B.G., Lucey, P.G., Jakosky, B.M., 1996. New laboratory measurements of mid-IR emission spectra of simulated planetary surfaces. *J. Geophys. Res.* 101, 14969–14975.
- Houck, J.R. et al., 2004. The Infrared Spectrograph (IRS) on the Spitzer Space Telescope. *Astron. Phys. J. Suppl.* 154, 18–24.
- Ivezić, Ž. et al. the SDSS Collaboration, 2001. Solar System objects observed in the Sloan Digital Sky survey commissioning data. *Astron. J.* 122, 2749–2784.
- Klima, R.L., Pieters, C.M., Dyar, M.D., 2005. Pyroxene spectroscopy: Effects of major element composition on near, mid and far-infrared spectra. In: Mackwell, S., Stansbery, E. (Eds.), *36th Annual Lunar and Planetary Science Conference*, Lunar and Planetary Inst. Technical Report (Abstract #1462).
- Klima, R.L., Pieters, C.M., Dyar, M.D., 2007. Spectroscopy of synthetic Mg-Fe pyroxenes I: Spin-allowed and spin-forbidden crystal field bands in the visible and near-infrared. *Meteorit. Planet. Sci.* 42, 235–253.
- Lazzaro, D., Angeli, C.A., Carvano, J.M., Mothé-Diniz, T., Duffard, R., Florczak, M., 2004. 5°S^2 : The visible spectroscopic survey of 820 asteroids. *Icarus* 172, 179–220.
- Lebofsky, L.A., Sykes, M.V., Tedesco, E.F., Veeder, G.J., Matson, D.L., Brown, R.H., Gradie, J.C., Feierberg, M.A., Rudy, R.J., 1986. A refined 'standard' thermal model for asteroids based on observations of 1 Ceres and 2 Pallas. *Icarus* 68, 239–251.
- Lim, L.F., McConnochie, T.H., Bell, J.F., Hayward, T.L., 2005. Thermal infrared (8–13 μm) spectra of 29 asteroids: The Cornell Mid-Infrared Asteroid Spectroscopy (MIDAS) survey. *Icarus* 173, 385–408.
- Logan, L.M., Hunt, G.R., Salisbury, J.W., Balsamo, S.R., 1973. Compositional implications of Christiansen frequency maximums for infrared remote sensing applications. *J. Geophys. Res.* 78 (23), 4983–5003.
- Masiero, J., Jedicke, R., Durech, J., Gwyn, S., Denneau, L., Larsen, J., 2009. The thousand asteroid light curve survey. *Icarus* 204, 145–171.
- Matson, D.L., 1972. Infrared Emission from Asteroids at Wavelengths of 8.5, 10.5 and 11.6 Millimicron. Ph.D. Thesis, California Institute of Technology.
- McCord, T.B., Adams, J.B., Johnson, T.V., 1970. Asteroid Vesta: Spectral reflectivity and compositional implications. *Science* 178, 745–747.
- Mittlefehldt, D.W., 1994. The genesis of diogenites and HED parent body petrogenesis. *Geochim. Cosmochim. Acta* 58, 1537–1552.
- Mittlefehldt, D.W., 2008. Meteorite Dunite Breccia MIL 03443: A probable crustal cumulate closely related to diogenites from the HED parent asteroid. In: *Lunar and Planetary Institute Science Conference Abstracts*. Lunar and Planetary Inst. Technical Report, vol. 39 (Abstract # 1919).
- Mittlefehldt, D.W., McCoy, T.J., Goodrich, C.A., Kracher, A., 1998. Non-chondritic meteorites from asteroidal bodies. In: Papike, J.J. (Ed.), *Planetary Materials, Reviews in Mineralogy*, vol. 36. Mineralogical Society of America, Washington, DC.
- Mittlefehldt, D.W., Beck, A.W., Lee, C., McSween, H.Y., 2009. Chemistry of diogenites and evolution of their parent asteroid. In: *Lunar and Planetary Institute Science Conference Abstracts*. Lunar and Planetary Inst. Technical Report, vol. 40 (Abstract # 1038).
- Moskovitz, N.A., Jedicke, R., Gaidos, E., Willman, M., Nesvorný, D., Fevig, R., Ivezić, Ž., 2008. The distribution of basaltic asteroids in the main belt. *Icarus* 198, 77–90.
- Moskovitz, N.A., Willman, M., Burbine, T.H., Binzel, R.P., Bus, S.J., 2010. A spectroscopic comparison of HED meteorites and V-type asteroids in the inner main belt. *Icarus* 208, 773–788.
- Nesvorný, D., Roig, F., Gladman, B., Lazzaro, D., Carruba, V., Mothé-Diniz, T., 2008. Fugitives from the Vesta family. *Icarus* 193, 85–95.
- Pieters, C.M., Binzel, R.P., Bogard, D., Hiroi, T., Mittlefehldt, D.W., Nyquist, L., Rivkin, A., Takeda, H., 2006. Asteroid-meteorite links: the Vesta conundrum(s). In:

- Daniela, L., Sylvio Ferraz, M., Angel, F.J. (Eds.), *Asteroids, Comets, Meteors*. IAU Symposium, vol. 229, pp. 273–288.
- Rayner, J.T., Toomey, D.W., Onaka, P.M., Denault, A.J., Stahlberger, W.E., Vacca, W.D., Cushing, M.C., Wang, S., 2003. SpeX: A medium-resolution 0.8–5.5 micron spectrograph and imager for the NASA infrared telescope facility. *Publ. Astron. Soc. Pacific* 115, 362–382.
- Salisbury, J.W., D'Aria, D.M., Jarosewich, E., 1991. Midinfrared (2.5–13.5 microns) reflectance spectra of powdered stony meteorites. *Icarus* 92, 280–297.
- Smith, J.A. et al., 2002. The u'g'r'i'z' standard-star system. *Astron. J.* 123, 2121–2144.
- Spencer, J.R., 1990. A rough-surface thermophysical model for airless planets. *Icarus* 83, 27–38.
- Spencer, J.R., Lebofsky, L.A., Sykes, M.V., 1989. Systematic biases in radiometric diameter determinations. *Icarus* 78, 337–354.
- Sunshine, J.M., Pieters, C.M., 1993. Estimating modal abundances from the spectra of natural and laboratory pyroxene mixtures using the modified Gaussian model. *J. Geophys. Res.* 98, 9075–9087.
- Sunshine, J.M., Pieters, C.M., Pratt, S.F., 1990. Deconvolution of mineral absorption bands – An improved approach. *J. Geophys. Res.* 95, 6955–6966.
- Sunshine, J.M., Bus, S.J., McCoy, T.J., Burbine, T.H., Corrigan, C.M., Binzel, R.P., 2004. High-calcium pyroxene as an indicator of igneous differentiation in asteroids and meteorites. *Meteorit. Planet. Sci.* 39, 1343–1357.
- Tedesco, E.F., Veeder, G.J., Fowler, J.W., Chillemi, J.R., 1992. The IRAS Minor Planet Survey. Tech. Rep. PL-TR-92-2049, Phillips Laboratory, Hanscom Air Force Base, MA.
- Tedesco, E.F., Noah, P.V., Noah, M., Price, S.D., 2002. The supplemental IRAS minor planet survey. *Astron. J.* 123, 1056–1085.
- Thomas, P.C., Binzel, R.P., Gaffey, M.J., Storrs, A.D., Wells, E.N., Zellner, B.H., 1997a. Impact excavation on Asteroid 4 Vesta: Hubble Space Telescope results. *Science* 277, 1492–1495.
- Thomas, P.C., Binzel, R.P., Gaffey, M.J., Zellner, B.H., Storrs, A.D., Wells, E., 1997b. Vesta: Spin pole, size, and shape from HST images. *Icarus* 128, 88–94.
- Turnock, A., Lindsley, D., Grover, J., 1973. Synthesis and unit-cell parameters of Ca–Mg–Fe pyroxenes. *Am. Mineral.* 58 (1–2), 50–59.